CrystEngComm

PAPER

View Article Online
View Journal | View Issue

Cite this: *CrystEngComm*, 2025, **27**, 4965

Controlled microcrystallization for *in situ* photocrystallography: optimizing crystal size and habit†

Sam G. Lewis, [ab] Ben A. Coulson,[a] Kenneth D. M. Harris, [a] Anna J. Warren, [b] Mark R. Warren [b] and Lauren E. Hatcher *[a]

While advanced crystallization methods controlling microcrystal size and shape are common for pharmaceutical targets, there are few examples where such methods are applied to inorganic functional materials. This is surprising, considering the impact of particle size on numerous useful properties. As an archetypal photoswitch exhibiting photoinduced linkage isomerism (PLI), sodium nitroprusside dihydrate (SNP·2H_2O) is an ideal prototype for the design of advanced inorganic microcrystallization approaches. Slow evaporation in water characteristically gives long (>1 mm) lath-like crystals with a broad size distribution. These samples are undesirable for *in situ* photocrystallography, where small crystals of ideally plate habit are preferred to maximize light penetration. This article explores the influence of solvent, temperature and crystallization method on the formation of homogeneous microcrystal batches of SNP·2H_2O at small (*ca.* 5 mL) scale, targeting a plate-like habit and an average size of (50 ± 10) μm in the two dimensions parallel to the plate. Successful experiments utilize an acetonitrile antisolvent methodology, delivering a narrow crystal size distribution in the correct range. Steady-state photocrystallography measurements on crystals grown by controlled *vs.* uncontrolled methodologies showcase how regulating crystal particle attributes can minimise variability in the excited state population, reinforcing the importance of these parameters for real photoswitching applications where achieving a reproducible response is often key. A previously unknown mixed methanol : water solvate of SNP is also reported that is metastable in air.

Received 3rd April 2025,
Accepted 23rd June 2025

DOI: 10.1039/d5ce00367a

rsc.li/crystengcomm

Introduction

The rise in *in situ* structural studies on switchable crystals over the last two decades has generated an increased understanding of the key structure–property relationships that underpin various applications including optoelectronics, data storage, battery science and sustainable technologies *e.g.* gas storage and solar energy conversion.[1–6] Whilst it is well-established that systematic modification of the chemical structure of a photoswitching molecule can tune its useful chemistry, in recent decades there has been a concerted effort to also understand how changes in the crystal packing can influence solid-state properties.[7–13] This is a challenging problem as, despite tailored crystal engineering approaches aimed at controlling intermolecular interactions to promote particular packing motifs,[8] it remains difficult to predict and control the full crystal structure in three-dimensions. Thus, it is rare that two analogous switchable molecules crystallize into isostructural phases that allow direct comparison of their structure–property correlations. Equally challenging is the goal of quantifying how macroscale attributes, such as crystal/particle size and habit, can impact on useful behaviours. Particle size has a significant impact on the useful properties of various functional materials, from the mechanical properties of extended materials such as metals, alloys and metal–organic frameworks (MOFs),[14–17] to domain-dependent properties such as magnetic and ferroelectric switching.[18,19] For photoswitchable crystals, controlling the crystal size and shape is beneficial to ensure that the incident excitation light penetrates through the crystal bulk. Small crystals with ideally plate-like habits are typically preferable, as irradiation in a direction parallel to the shortest dimension of a plate will maximize the penetration of light through the crystal. Thus, photocrystallography experiments, in which a crystal is irradiated *in situ* whilst single crystal X-ray diffraction (SCXRD) data are recorded, have traditionally been performed on the

[a] *School of Chemistry, Cardiff University, Cardiff, CF10 3AT, UK. E-mail: HatcherL1@cardiff.ac.uk*
[b] *Diamond Light Source, Harwell Science and Innovation Campus, Didcot, Oxfordshire, OX11 0DE, UK*

† Electronic supplementary information (ESI) available: 1. PDF ESI Sections 1–6. 2. Raw FT-IR, PXRD and photocrystallography data. CCDC 2440144. For ESI and crystallographic data in CIF or other electronic format see DOI: https://doi.org/10.1039/d5ce00367a

smallest crystals and using the brightest X-ray sources available.[20,21] This often leads to issues such as X-ray and light damage,[22] making it desirable to perform repeat data collections on several different single crystals. To overcome such issues, and in line with the recent and global trend to upgrade synchrotron X-ray facilities and build new ultrabright X-ray free electron laser (XFEL) facilities,[23–26] new multi-crystal methodologies such as serial crystallography (SX) are attracting attention. These "diffract-before-destroy" approaches involve the delivery of many hundreds, or even thousands, of microcrystals into the X-ray beam so that a single image is collected on each crystal. The data from all suitable crystals are then combined and used for crystal structure determination. A key obstacle for multi-crystal methods is the need to produce the many highly-crystalline, single microcrystals required for delivery into the X-ray beam. Although scaling methods can be applied to address the variation in diffraction power from crystals of different size or habit, such scaling will always reduce the quality of the final merged dataset. Furthermore, for *in situ* experiments such as photocrystallography,[22] the need for homogeneous microcrystal batches becomes especially important due to the reasons outlined above.[27]

Despite the obvious importance of the crystal size and habit for photocrystallography and SX, systematic studies investigating the parameters needed to control these attributes in switchable functional materials are scarce. Similarly, there exist only a few reports focused solely on the direct preparation of reproducible batches of microcrystals for SX for any type of material,[28,29] and many studies have relied on post-processing steps to achieve a narrow size distribution. This approach is not always desirable, as extra processing steps can cause attrition, breakage, or changes in the crystal phase, while crystal sorting processes, *e.g.* sieving, are inherently wasteful and so preclude the study of precious samples. The latter point is particularly relevant to functional photoswitches, which are often composed of high-value metal and/or organic ligand moieties and accessed *via* complicated multi-step synthetic procedures. In such cases, it is better to tailor the primary crystallization process to directly produce microcrystal batches of the desired habit and size.

We herein present a crystallization strategy to generate microcrystal batches of an archetypal inorganic photoswitch, sodium nitroprusside dihydrate (Fig. 1, SNP·2H_2O = $Na_2[Fe_1C_5N_6O_1]\cdot 2H_2O$) of narrow size distribution and identical habit. Our approach adopts methods most commonly utilized for pharmaceutical crystallizations,[30–32] where the tight control of crystal particle attributes can be critical for physicochemical properties (*e.g.* dissolution, stability) and for downstream particle processing. While the advanced control of primary crystallization processes is commonplace for pharmaceuticals, the controlled crystallization of functional photoswitches such as SNP·2H_2O is under-researched and is an area of crystallization with significant potential for future development. To the best of our knowledge, SNP·2H_2O is the only known crystal form of the di-sodium salt of nitroprusside, with no other polymorphs or solvates currently reported.

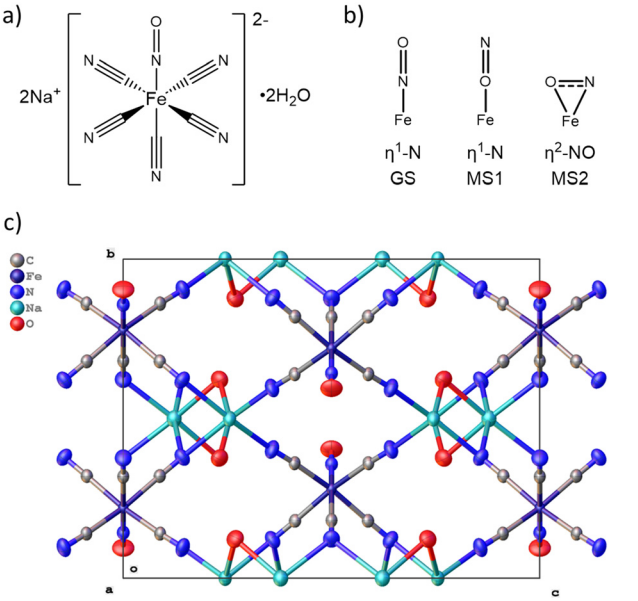

Fig. 1 a) The molecular structure of sodium nitroprusside dihydrate (SNP·2H_2O), b) the binding modes of the ground state (GS), metastable 1 (MS1) and metastable 2 (MS2) states, and c) the crystal structure of SNP·2H_2O (ICSD 8214, CSD DOJJAP), viewed along [100] with hydrogen atoms omitted for clarity (Fe = dark blue, Na = light blue, C = grey, N = dark blue and O = red).

SNP·2H_2O exhibits unusually long-lived metastable states, MS1 and MS2, as a result of photoinduced linkage isomerism (PLI) of the nitrosyl ligand (Fig. 1b). The subject of the first reported photocrystallographic study by Coppens *et al.* in 1997,[33] the structure of the photoinduced, η^1-ON isomer was accessed on irradiation of a single crystal with 488 nm laser light at 50 K. The excited crystal was then further irradiated with 1064 nm light to convert MS1 into the side-on bound η^2-O,N MS2 isomer, with prolonged infrared irradiation causing depopulation back to the η^1-NO ground state. The system crystallizes into large and often intergrown[34] crystals that are poorly suited for photocrystallographic studies. Thus, we here develop a crystallization procedure for producing monophasic batches of SNP·2H_2O microcrystals with a narrow crystal size distribution and a uniform plate-like habit that are tailored for *in situ* photocrystallography. The target crystal size is in the range (50 ± 10) μm in the two dimensions parallel to the plate, which was chosen to match the fixed-target grid size for state-of-the-art SX measurements that have been developed using these crystals, in parallel with this study.[35,36] This size range is also a suitable compromise between maximizing the photoexcited state population and obtaining sufficient diffraction intensity using a modern microfocus rotating anode laboratory X-ray source, or a synchrotron X-ray beam.

Experimental

Materials

SNP·2H_2O was purchased from Thermo Fisher Scientific and ground into a powder using a pestle and mortar prior to all

crystallization experiments. Methanol, ethanol, acetonitrile, and tetrahydrofuran solvents were purchased from Fisher Scientific and were used without further purification. All manipulations were carried out in air, unless otherwise stated.

Full methods for all the analytical techniques used in this article are recorded in the ESI† (Section S1).

Summary of crystallization experiments

In the progress of this work a large number of exploratory crystallization experiments were conducted including evaporative, antisolvent and cooling approaches that utilized fast and slow methods to approach supersaturation. Tables 1 and 2 summarize the breadth of these experiments and herein the discussion focuses on the most successful routes, which are discussed in detail. The choice of solvents was made on account of the limited solubility of SNP·2H_2O, which was only significantly soluble in deionized water and sparingly soluble in short chain alcohols, tetrahydrofuran and acetonitrile. Gravimetric solubility measurements were conducted, for which suitable data were obtained only in deionized water and methanol (see ESI† Section S2). Slow evaporation experiments from methanol and ethanol, slow vapor diffusion experiments and both slow and fast cooling crystallizations were all informative design steps towards the final crystallization process, but did not yield microcrystals of the desired size distribution (50 ± 10) μm or the ideal plate-like habit. As such, these experiments are not discussed here but are described thoroughly in the ESI:† Section S2 summarizes the gravimetric solubility data; Section S3† the slow evaporation experiments; Section S4† the fast (drop casting) evaporation studies; Section S5† the antisolvent crystallizations; and Section S6† provides full details of all cooling crystallizations.

Slow evaporative crystallization

A small portion of SNP·2H_2O (10 mg, 0.03 mmol) was placed into a crystallization vial and fully dissolved in 1 mL of deionized water to create an undersaturated solution. The solution was then filtered through a glass pipette, packed with 1 cm of cotton wool, into a clean crystallization vial and capped with a lid containing 5 holes. The vial was placed in the dark and the solvent allowed to evaporate slowly until crystals had formed, over a period of 2 days.

Fast evaporative crystallization (drop casting)

A saturated aqueous solution (0.66 g g^{-1}) was prepared by dissolving SNP·2H_2O (3.3 g, 11.1 mmol) in deionized water (5 mL) was stirred at 500 RPM for 1 h at 60 °C. The stirring was then stopped and the temperature held whilst any excess solid was allowed to settle at the bottom of the vial. An aliquot of the supernatant was then filtered through a glass pipette, packed with 1 cm of cotton wool heated to 60 °C in an oven, into a clean vial at 60 °C. For the drop-casting procedure, a small aliquot of the solution was transferred in a pre-heated glass pipette to a microscope slide and left uncovered to allow fast evaporation to dryness, which occurred over a period of 60 s. Crystal growth within the droplet was visualized by polarized light microscopy and images were recorded throughout crystal formation.

Fast antisolvent crystallization

An aqueous solution (0.48 g g^{-1}) was prepared by dissolving SNP·2H_2O (1.44 g, 4.83 mmol) in deionized water (3 mL), then heated to 40 °C and stirred at 500 RPM for 0.5 h to allow for full dissolution. Acetonitrile (1 mL) was simultaneously heated and held at 40 °C. The stirring rate was reduced to 100 RPM and 0.1 mL of the SNP solution was quickly transferred into the acetonitrile antisolvent in a time period of 1 s using a fixed-volume micropipette. Stirring of the mixture was continued for 5 min to allow for crystal formation, then a small aliquot of the crystal-containing solution was transferred to a microscope slide and a coverslip placed over the droplet for inspection by polarized light microscopy. Crystals were then recovered by vacuum filtration for powder X-ray diffraction (PXRD),

Table 1 Summary of the results from evaporative and cooling crystallization experiments conducted with SNP·2H_2O from single solvent media, with reference to the crystal habit, the size range of the maximum crystal dimension and the phase purity of the product

Method →	Evaporative		Cooling	
Solvent ↓	Slow	Fast	Slow	Fast
Water	Thick laths	Thin laths	Laths	Thin laths
	100–1500 μm	10–150 μm	30–70 μm	150–200 μm
	Monophasic	Monophasic	Monophasic	Monophasic
Methanol	Thin laths	Square plates	Thin laths	Plates
	150–500 μm	20–40 μm	10–30 μm	10–30 μm
	Monophasic	Biphasic[a]	Monophasic	Biphasic[a]
Ethanol	Laths	Thin laths	Thin laths	Thin laths
	100–1000 μm	<10 μm	<10 μm	<10 μm
	Monophasic	Monophasic	Monophasic	Monophasic

[a] Biphasic samples were confirmed to contain a new mixed methanol : water solvate, in addition to the known SNP·2H_2O phase, as discussed *vida infra*.

Table 2 Summary of results from antisolvent crystallization experiments conducted with SNP·2H$_2$O, with reference to the crystal habit, the size range of the maximum crystal dimension and the phase purity of the product

Solvent/antisolvent	Slow	Fast
Water/ethanol	Blocks, 100–1000 μm, monophasic	Short laths, 10–30 μm, monophasic
Water/acetonitrile	[b]	Plates, 30–70 μm, monophasic
Water/tetrahydrofuran	[b]	Plates, 10–150 μm, monophasic
Methanol/ethanol	Square plates, 80–120 μm, biphasic[a]	[c]
Methanol/acetonitrile	Non-single, 50–120 μm, monophasic	[c]

[a] Biphasic samples were confirmed to contain a new mixed methanol : water solvate, in addition to the known SNP·2H$_2$O phase, as discussed *vida infra*. [b] Indicates no crystals were formed under these experimental conditions. [c] Indicates that no experiment was conducted in this parameter space.

Fourier transform infrared (FT-IR) spectroscopy, and face-indexing by SCXRD.

Results and discussion

Slow evaporative crystallization from water

Initial batch crystallizations were conducted by slow evaporation of an undersaturated aqueous solution of SNP·2H$_2$O. These experiments provided an understanding of the natural crystal habit before any controlled crystallization approach was applied. The gravimetric solubility data obtained for SNP·2H$_2$O in deionized water (Fig. S1 and Table S1†), were used to inform the preparation of undersaturated solutions. The crystals formed were predominantly large laths of a very broad, asymmetric size distribution and high aspect ratios (Fig. 2 and S3†), with a tendency to exhibit intergrowth behaviour. Analysis of the bulk crystallized sample by PXRD and FT-IR spectroscopy (Fig. S4 and S5†) confirmed that only the known SNP·2H$_2$O phase was produced.

A representative non-intergrown crystal prepared by slow evaporation of water was analysed by SCXRD to better understand the rates of natural facet growth in water with respect to the underlying crystal structure. The unit cell parameters determined (a = 6.2014(17) Å, b = 11.883(4) Å, c = 15.584(4) Å, α = 90°, β = 90°, γ = 90°) matched those of the

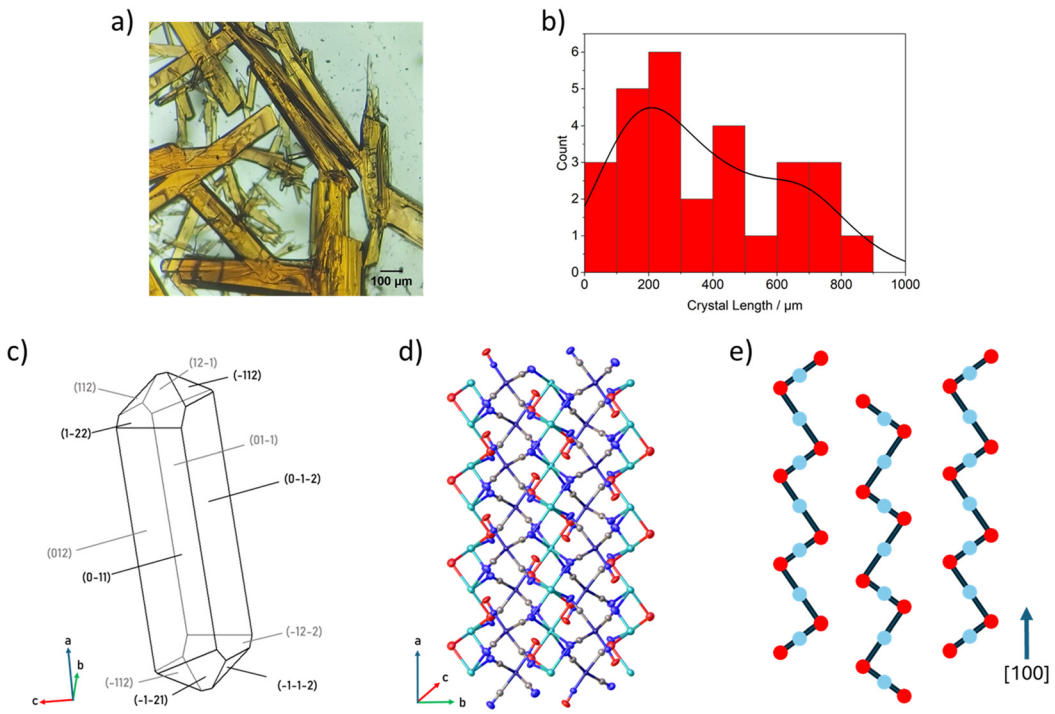

Fig. 2 Crystals formed by slow evaporative crystallization of SNP·2H$_2$O from deionized water, a) optical micrograph showing crystals of SNP·2H$_2$O formed with an average length of 375(239) μm and an average aspect ratio of 6(2), b) crystal size distribution (longest dimension) measured by optical micrographs for 28 crystals in the displayed image, histogram bin width = 100 μm, c) natural crystal faces of a representative crystal and the corresponding unit cell axes, crystal particle form classified as prolate using Zingg analysis (see Fig. S37†), d) the SNP·2H$_2$O crystal structure (ICSD 8214, CSD DOJJAP) with hydrogen atoms omitted for clarity and with the [100] direction vertical, and e) illustration of the sodium···water chains (red = O, light blue = Na) in the structure parallel to [100], viewed along the c axis with the [100] direction vertical. In d) and e), Fe = dark blue, Na = light blue, C = grey, N = blue and O = red.

known SNP·2H_2O structure (Cambridge Structural Database entry ID DOJJAP;[37] and Inorganic Crystal Structure Database[38] collection code 8214), in agreement with the PXRD analysis. The natural crystal faces, determined experimentally by face indexing of this crystal, are represented in Fig. 2c. Using the 3D crystal particle dimensions determined from face indexing, classification of the crystal morphology presented in Fig. 2c was made using the Zingg approach, which identifies the particle form as prolate.[39] Details of the Zingg approach and visualizations of the crystal form assignments for this study are provided in Section S9 of the ESI.†

The longest crystal dimension coincides with the crystallographic *a* axis, indicating preferential crystal growth along the [100] direction. Interestingly, the capping faces are not the (100) and (−100) planes, but instead the {112}, {121} and {122} sets appear most prominently at the crystal ends to generate a prismatic morphology. To better understand the higher relative growth rate along [100], the experimentally-determined prolate crystal habit was overlaid with the bulk crystal structure in the CCDC software Mercury (Fig. S6†).[40] X-ray diffraction is a bulk structure determination technique and therefore does not allow for direct visualization of the functional groups or framework components that are present at the crystal surfaces. However, plausible inferences regarding the likely surface terminations may be made from analysis of the bulk crystal structure.[30] In this regard, an approach to rationalize preferential growth along [100] is to consider the key intermolecular interactions that propagate along this direction in the bulk crystal structure. A key feature of the SNP·2H_2O crystal structure is the presence of chains of sodium cations and water molecules that extend parallel to the longest crystal dimension and the [100] direction (Fig. 2d and e). It is likely that the formation of strong coordination bonds between the polar water molecules and the sodium cations in these chains is the fastest mechanism of crystal growth for SNP·2H_2O in deionized water, and hence this provides a credible mechanism for the observed preferential growth along [100].

It follows that modification of the crystallization conditions, such that the formation of these sodium···water chains is disrupted, may act to retard the crystal growth along [100] and thereby effect a change in the crystal habit. An obvious approach would be to reduce the water content, *e.g.* through the introduction of different solvents or antisolvents. Accordingly, slow evaporative crystallization experiments from other solvents (methanol and ethanol) were investigated (Table 1) but did not show a significant improvement in the target crystal attributes. These experiments are discussed in more detail in the ESI† (Section S3 and Fig. S7–S9).

Fast evaporative crystallization (drop casting)

Drop casting crystallization experiments were performed using saturated solutions of SNP·2H_2O in deionized water. Saturated solutions were prepared in reference to the gravimetric solubility data (Fig. S1, Table S1†). The faster evaporation rate used in these experiments aimed to promote rapid nucleation by quickly increasing the supersaturation level in the solution, which in turn promotes a faster nucleation rate to deliver a larger number of smaller individual crystals than is observed by slow evaporation.[41] The results of these experiments are visualized in Fig. 3a. Drop cast aqueous solutions did not give rise to a change in the crystal habit and still produced elongated habits with a high average aspect ratio of 7(3). However, the crystal size was markedly reduced, with an average length of the longest crystal dimension of 119(53) μm, and the size distribution was narrower in comparison to the products obtained by slow evaporation from water (Fig. 3b and S11†). Despite this improvement, the crystal size distribution is still not within the target range and, overall, the results show that the crystal attributes are still not optimized.

Drop casting experiments were also performed from saturated solutions in ethanol and methanol (Table 1), which both resulted in a reduction in the crystal size distribution. However, other requirements for the target application were not achieved, including control over the crystal habit and the phase purity. These results are

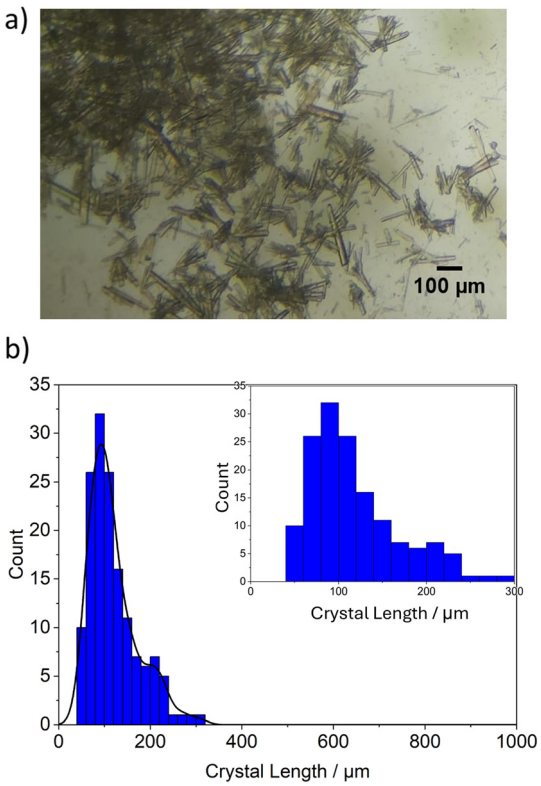

Fig. 3 Crystals formed by fast evaporation (drop casting) of an aqueous solution of SNP·2H_2O, a) optical micrograph showing crystals of SNP·2H_2O formed with an average length of 119(53) μm and average aspect ratio of 7(3), b) crystal size distribution (longest dimension) measured in optical micrographs for 150 crystals in the displayed image, histogram bin width = 20 μm. The inset shows a magnified view of the region of interest for crystal lengths between 0 and 300 μm.

discussed in more detail in the ESI† (Section S4, Fig. S10 and S12–S14).

Antisolvent crystallization

The success of rapid evaporative (drop casting) methods in producing crystals much closer to the target crystal dimensions of (50 ± 10) μm informed the design of an antisolvent crystallization method in which a saturated aqueous solution of SNP·2H_2O was swiftly injected into an antisolvent with stirring, causing the rapid precipitation of crystals. It is expected that fast mixing with the antisolvent will lead to a rapid decrease in the solubility of SNP·2H_2O, promoting fast nucleation and the production of many, small microcrystals. As such, various water miscible antisolvents were tested, with the most promising crystal batches obtained using acetonitrile, ethanol, and tetrahydrofuran as antisolvents (Table 2 and Fig. S15†).

Crystals produced with acetonitrile as the antisolvent (Fig. S15a†) predominantly display a rectangular plate-like habit, with a markedly reduced crystal size on the order of 30–70 μm in the two dimensions of the plate, which approach the target size parameters. Visual inspection with polarized light microscopy confirmed the formation of good quality single crystals that extinguish evenly under crossed-polarized light.[42] The use of ethanol as the antisolvent (Fig. S15b†) produced lath-like microcrystals smaller than the target size range, whilst the use of tetrahydrofuran as the antisolvent (Fig. S15c†) produced microcrystals that were heavily agglomerated and displayed a broad size distribution. All products were tested by PXRD and FT-IR (Fig. S16 and S17†), which confirmed that they were monophasic samples of SNP·2H_2O.

Optimization of the fast antisolvent crystallization procedure

Assessment of all the crystal batches detailed in this study (Tables 1 and 2) showed that the fast antisolvent crystallization procedure using acetonitrile produced the most promising microcrystals. However, some variability in the crystal size and habit produced by this method was still evident. The method was further refined by investigating a range of conditions, including temperature and the concentration of the aqueous solution of SNP·2H_2O, targeting product microcrystals with identical plate-like habits across the batch and a narrower size distribution. The concentrations of the SNP·2H_2O solutions were chosen in reference to the gravimetric solubility data in deionized water (Table S1 and Fig. S1†) and aimed for slightly undersaturated solutions at concentrations just below the solubility limit at 30 °C, 40 °C and 50 °C, respectively. The resultant microcrystal batches formed in this optimization study are shown in Fig. 4 and S18.†

Crystallization at 40 °C with the aqueous solution of SNP·2H_2O at a concentration of 0.44 g g^{-1} produced the best batch of rectangular plate-like crystals, with an average aspect ratio of 1.4(4) and a narrow size distribution with an average crystal size of 51(8) μm in the longest dimension (Fig. 4 and S19†). These crystal attributes entirely match the target parameters, and PXRD and FT-IR (Fig. S20 and S21†) confirm that all of the microcrystal batches produced in this optimization study were monophasic samples of SNP·2H_2O. For comparison to the original prolate crystal habit of SNP·2H_2O (Fig. 2c), face indexing of a representative crystal prepared by fast antisolvent crystallization from acetonitrile under the optimal conditions was carried out by SCXRD (Fig. 4c). The experimentally-determined crystal faces confirm that growth along [100], which is the prominent direction in the prolate crystal habit grown by slow evaporation, is significantly reduced relative to growth along [010] under these optimized conditions. This produces a different crystal habit, with approximately equal crystal dimensions parallel to the crystallographic *a* and *b* axes that is characterised as an oblate habit *via* Zingg analysis (ESI Section S9†).[39]

The largest crystal facets are (001) and (00−1), with the slowest growth and shortest crystal dimension parallel to the *c*-axis. Overlaying the SNP·2H_2O crystal structure with this oblate habit (Fig. S22†) again allows a qualitative rationalization of the crystal shape. The reduction in the relative growth rate along [100] can potentially be explained by the presence of an excess of acetonitrile antisolvent under these conditions, which will necessarily limit the availability of water molecules to form the sodium···water chains that dominate the structure in this direction (Fig. 2e). Moreover, it is possible that acetonitrile may compete with water for coordination along the direction dominated by sodium···water coordination bonds (*i.e.* [100] as identified in Fig. 2) and may therefore selectively inhibit growth along [100] while not significantly altering the growth rate in other directions. From the crystal structure it is apparent that relative promotion of growth along [010] is not heavily dependent on the water content. Instead, the dominant interactions in this direction are sodium···cyano coordination bonds forming a "wine-rack"-like pattern of {Na–CN–Fe} units in the *bc* plane (Fig. 4e and S22†). This indicates that the formation of sodium···cyano coordination bonds is likely to be the dominant growth mechanism along [010], which should be comparatively unaffected by the solvent/antisolvent composition.

Crystals from the optimal microcrystal batch, generated by fast antisolvent mixing of SNP·2H_2O (0.44 g g^{-1}) with acetonitrile at 40 °C, were further analysed by scanning electron microscopy (SEM) (Fig. 4d). These measurements further confirmed the crystal habit observed by polarized light microscopy and SCXRD face indexing methods and determined a representative three-dimensional crystal size of 50 × 25 × 10 μm^3.

In situ photocrystallography

A series of *in situ* photocrystallography experiments was performed to assess the impact of controlling the crystal particle attributes on the reproducibility of the photoexcited

state population. A sample of three crystals from the controlled, fast antisolvent methodology (Fig. 4a), classified as oblate, were tested and compared to a sample of three crystals grown by uncontrolled evaporation from water (Fig. 2a), classified as blade-like habits by Zingg analysis (Fig. S38†). Each set of three crystals were taken from the same batch, prepared *via* the indicated crystallization method. Each crystal was cooled to 100 K and subjected to irradiation using 465 nm LED light. After 1 h irradiation was stopped, the crystal was held in the dark at 100 K and a complete SCXRD dataset was collected to determine the photoexcited state population. Table 3 outlines the results from these steady-state photocrystallography studies. For all crystals, inspection of the photodifference maps (constructed as described in ESI† Section S1) only provided evidence of the isonitrosyl, MS1 isomer, hence the refined population values refer only to MS1. The results show that the excited state population achieved across the sample of oblate crystals is very reproducible, with an average MS1 population of 11(1)% (Table 3) and only a very small variation of 10(3)% to 12(3)% across the sample, which is negligible compared to the error on the refined occupancies of the nitrosyl ligand. By comparison, the excited state populations achieved for the blade-like crystals show slightly more variation, ranging from 11(3)% to 16(3)%. The average excited state populations for all crystals tested do not correlate with crystal size, which suggests that there is no significant benefit to using smaller crystals to maximise the steady-state MS1 population in SNP·2H_2O at 100 K. However, care should be taken in comparing the absolute values of the excited state populations, given that it is known that the maximum achievable population in crystals of SNP·2H_2O is heavily dependent on the direction that the incident light travels through the structure.[43] Therefore, the significant difference in crystal shapes, which alters the dominant facets that are most exposed to the light source, may significantly affect the maximum level of excitation achieved. Furthermore, these results compare only the steady-state population achieved by prolonged (1 h) exposure to low power, continuous wave LED light and thus do not reflect the influence that crystal size and habit may have on other commonly-used irradiation methods, *e.g.* high power pulsed laser systems with very short pulse durations.

In summary, the photocrystallographic results show that controlling the crystal particle attributes leads to a more reproducible photoexcited state population from crystal to crystal, although the trends seen in SNP·2H_2O are less pronounced than in some other systems.[27] It is often difficult to investigate the full parameter-space of a study (*e.g.* irradiation time, power, experiment temperature *etc.*) on only one crystal, when it is subject to repeated and prolonged X-ray and visible or UV light exposure that often causes irreparable damage to the sample. Thus, it is regularly necessary to perform repeat measurements on more than one crystal for even the least complicated of photocrystallographic studies. This is even more important in the context of state-of-the-art serial photocrystallography experiments, such as serial synchrotron crystallography (SSX) and serial femtosecond crystallography (SFX), that utilize the full power of ultrabright synchrotron and XFEL sources, respectively. These experiments use a diffract-before-destroy approach that involves the merging of individual frames of data collected on many hundreds, or even thousands, of crystals. By controlling the size and habit of the crystals that are introduced to the X-ray beam, the experimenter can be confident that one source of variability in their data is controlled, promoting a reliable photoexcited state population level in the final, merged dataset.

Mixed methanol/water solvate of SNP

Finally, it was observed that several crystallization routes using methanol produced crystals of varied habit (Tables 1 and 2) and PXRD and FT-IR analysis highlighted issues with

Table 3 Steady-state photocrystallography studies performed on plate crystals grown by either i) controlled, fast antisolvent methods, or ii) uncontrolled slow evaporation. Full details of crystal face indexing methods used to experimentally determine the crystal dimensions and volumes is provided in Section S1 of the ESI.†

Method →	Antisolvent				Slow evaporation			
Crystal repeat ↓	Crystal dimensions[a] min × mid × max (mm)	Crystal volume[a] (mm^3)	Ground state occupancy[b] (%)	MS1 occupancy[b] (%)	Crystal dimensions[a] min × mid × max (mm)	Crystal volume[a] (mm^3)	Ground state occupancy[b] (%)	MS1 occupancy[b] (%)
1	0.021 × 0.034 × 0.035	2.43×10^{-5}	88(3)	12(3)	0.089 × 0.135 × 0.505	496.22×10^{-5}	84(3)	16(3)
2	0.015 × 0.038 × 0.037	2.75×10^{-5}	89(3)	11(3)	0.102 × 0.178 × 0.321	414.60×10^{-5}	89(3)	11(3)
3	0.014 × 0.041 × 0.044	2.49×10^{-5}	90(3)	10(3)	0.078 × 0.135 × 0.398	354.30×10^{-5}	87(3)	13(3)
Mean	—	2.56×10^{-5}	89	11	—	421.71×10^{-5}	87	13
Standard deviation	—	0.14×10^{-5}	0.8	0.8	—	58.16×10^{-5}	2.1	2.1
Range	—	0.32×10^{-5}	2	2	—	141.92×10^{-5}	5	5

[a] Crystal dimensions and volumes were determined experimentally by crystal face-indexing. [b] Linkage isomer occupancies were refined freely from the SCXRD data *via* a standard disorder model using SHELX PART instructions.

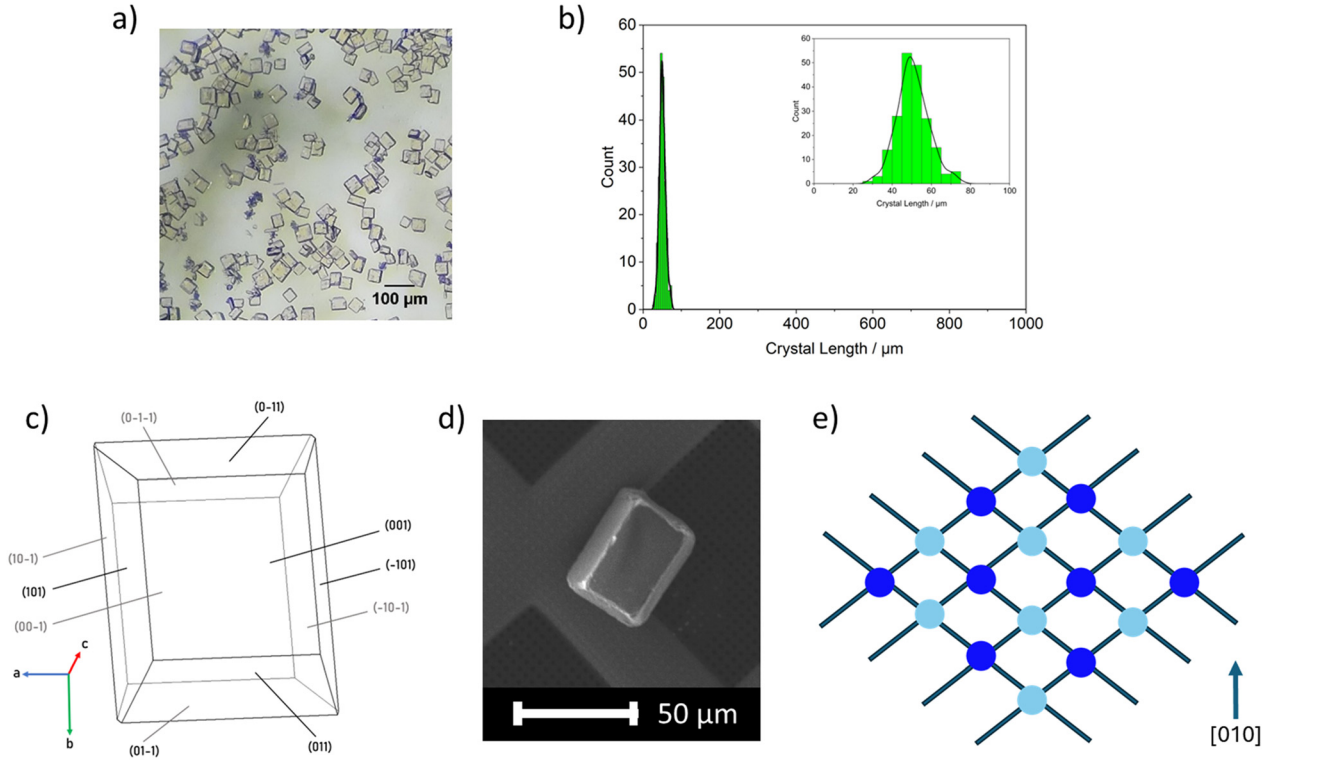

Fig. 4 a) Crystals formed by fast antisolvent mixing of acetonitrile with a 0.44 g g^{-1} aqueous solution of SNP·2H_2O at 40 °C [average crystal length 51(8) µm and average aspect ratio 1.4(4)], b) crystal size distribution (longest dimension) measured by optical micrographs for 200 crystals in the displayed image, histogram bin width = 5 µm, with the inset showing a magnified view of the region of interest for crystal lengths between 0 and 100 µm, c) natural crystal faces determined by single crystal face indexing, crystal particle form classified as oblate using Zingg analysis (see Fig. S37†), d) scanning electron micrograph of a representative oblate crystal grown by this method, and e) schematic diagram of iron (dark blue) and sodium (light blue) metal centres in the SNP·2H_2O crystal structure, viewed along the crystallographic *a*-axis with the [010] direction vertical, showing that crystal growth along [010] is dominated by the formation of sodium···nitroprusside coordination bonds.

the phase purity of these samples. Crystals grown by drop casting of saturated methanolic solutions (ESI† Section S4) initially formed with a plate habit, which rapidly redissolved over a period of 30 s and re-precipitated as laths (Fig. S12†). The final lath crystals were confirmed by further analysis to be the SNP·2H_2O phase (Fig. S13 and S14†). Similarly, crystals formed on slow cooling of undersaturated methanolic solutions (ESI† Section S6) also display a subtle habit variation, but again were found to exist only transiently. The FT-IR spectrum for these crystals displays significant differences to the FT-IR spectra obtained for phase pure SNP·2H_2O (Fig. S28†), typified by the appearance of a prominent new peak at 1001 cm^{-1} indicating the presence of a primary alcohol in the solid,[44] which suggests that methanol may be present in the crystal structure. PXRD analysis of the same crystal batch showed new peaks in addition to those expected for the known SNP·2H_2O phase (Fig. S29†), which further indicated that a new solvate structure had been formed. However, despite these interesting observations, it was not possible to isolate single crystals of this new phase from either the drop casting or slow cooling methods due to their transient nature.

A crystal suitable for SCXRD analysis was instead obtained by slow vapor diffusion of ethanol into a methanolic solution of SNP (ESI† Section S5 and Fig. S23b). This crystal was carefully removed from the vapor diffusion atmosphere and quickly mounted on a Kapton loop under a liquid nitrogen flow device at 150 K, enabling preservation of the crystal with the transient plate habit. Structure determination by SCXRD elucidated a previously unreported solid phase of SNP (Fig. 5 and Table 4), confirmed to be a water: methanol solvate that crystallizes in the monoclinic space group *I*2/*a*, with expanded unit cell dimensions in comparison to the known SNP·2H_2O structure. This new solvate incorporates one water molecule and one methanol molecule in the asymmetric unit, both fully-ordered and with anisotropic displacement parameters of comparable magnitude to the rest of the atoms in the structure, suggesting 100% occupancy in each case. The crystal data thereby support a 1 : 1 mixed solvent ratio. As in the structure of SNP·2H_2O, the water molecule adopts a bridging coordination between two sodium ions, while the coordinated methanol molecule is monodentate, which gives rise to a considerable change in the crystal packing arrangement. A detailed comparison of this new phase with the SNP·2H_2O structure is provided in the ESI† (Section S7 and Fig. S34). The transient nature of this mixed methanol : water phase is indicative that the crystals are hygroscopic, and readily

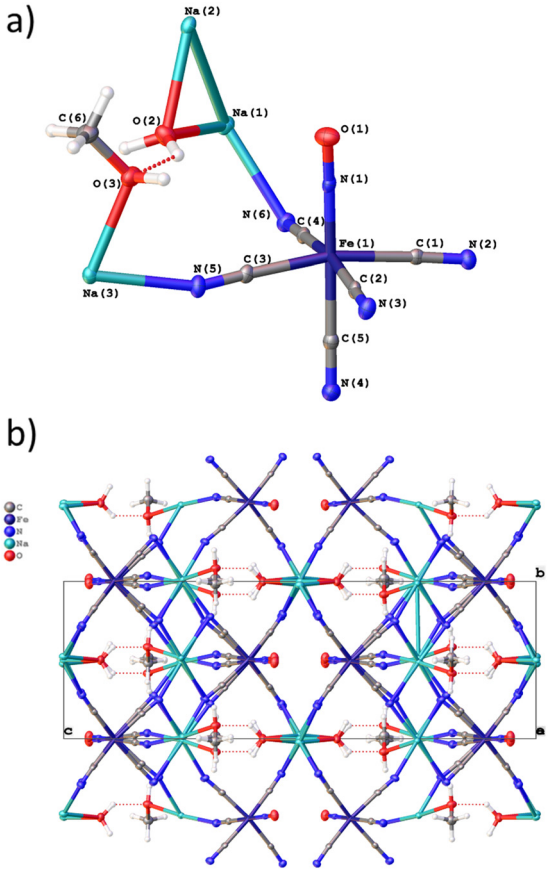

Fig. 5 a) The asymmetric unit of the mixed [1 : 1] methanol : water solvate of SNP and b) crystal structure observed along the crystallographic *a* direction. Ellipsoids are shown at 50% probability (Fe = dark blue, Na = light blue, C = grey, N = dark blue and O = red).

transform to the SNP·2H_2O phase under conditions where the water content cannot be minimized, which explains the difficulty in isolating the mixed methanol : water phase from most methanolic crystallization experiments in this study. This hypothesis is particularly evidenced by the observed transformation of plate crystals, grown by drop casting of saturated methanolic solutions, on aging for <1 minute in air (Fig. S12†).

Conclusions

We have successfully developed a small-scale crystallization strategy to deliver plate-like microcrystals of the archetypal photoswitch SNP·2H_2O with dimensions in the target size range of (50 ± 10) μm. A comparison of the crystal size distribution graphs in Fig. 2b–4b confirms the success of this strategy in refining the crystal size distribution, showing how advanced control of primary crystallization processes can be highly effective to manipulate the crystal attributes of functional inorganic photoswitches. The optimal fast antisolvent method has proven to be reproducible over multiple repeated crystallization experiments, with optical micrographs and crystal size distribution analysis performed on three batches, crystallized on 3 separate occasions, showing very little variation (ESI† Section S8, Fig. S35 and S36 and Tables S6–S8). The crystals generated have already been used for SSX experiments at Diamond Light Source, which are the subject of a separate publication.[36]

Table 4 Crystal data table for the [1 : 1] methanol : water SNP solvate

Empirical formula	$C_6H_6Fe_1N_6Na_2O_3$
Radiation	Cu Kα (λ = 1.54184 Å)
Formula weight	312
Temperature/K	100(1)
Crystal system	Monoclinic
Space group	*I*2/*a*
a/Å	12.9370(4)
b/Å	7.8904(2)
c/Å	24.4181(9)
α/°	90
β/°	104.462(4)
γ/°	90
Volume/Å^3	2413.57(14)
Z	8
ρ_{calc} g cm^{-3}	1.717
μ mm^{-1}	10.863
F(000)	1248.0
Crystal size/mm^3	0.05 × 0.05 × 0.01
Reflections (independent)	7110(2128)
Merging *R* statistics	R_{int} = 0.0249, R_{sigma} = 0.0264
Goodness-of-fit on F^2	1.047
R_1 [$I \geq 2\sigma(I)$]	0.0289
wR_2 [all data]	0.0867

The present study particularly highlights the effectiveness of experimental face-indexing methodologies and how an understanding of the natural crystal faces and their relationship with the underlying crystal structure can help to develop targeted crystallization routes, for example by promoting or inhibiting the relative growth rate along a particular direction to affect a change in crystal habit.

Finally, we present a previously unreported mixed [1 : 1] methanol : water phase of SNP, which is formed transiently from methanolic solvent media under conditions of low water content. The discovery of this new crystal form is a further reminder of the complex and often subtle role of the solvent, and of the interesting phase behaviour that may arise in the early stages of crystal nucleation and growth, which is overlooked when analysis is only performed on the final, stable product crystals. Further understanding of the nature of this transient phase and its evolution under differing crystallization conditions may be obtained by *in situ* analysis methods, for example using process analytical technology (PAT) methods such as in-line Raman spectroscopy, focused beam reflectance measurement (FBRM) and particle vision measurement (PVM), or by *in situ* diffraction studies. It was not possible to utilize PAT methods for this experiment as all crystallizations in this study were performed at small (*ca.* 5 mL) scale due to the requirements of the target SSX technique, whereas PAT typically requires a larger scale crystallization set-up. However, further studies focused on the crystallization of new solid forms of SNP should utilize such *in situ* approaches in the future.

Data availability

Crystallographic data for the novel mixed methanol : water SNP solvate structure reported in this article have been deposited at the Cambridge Crystallographic Data Centre under deposition number CCDC 2440144. Copies of the structure data can be obtained free of charge *via* **https://www.ccdc.cam.ac.uk/structures/**. Due to their size, raw data frames for all the crystal structure data reported in this article are archived and are available from the authors on reasonable request. All other relevant data generated and analysed in this article, including additional methods, spectroscopic data, powder X-ray diffraction patterns, additional crystallographic data and crystal face indexing information (in CIF format), crystal measurement and size distribution statistics are available in this article and its ESI† in the following formats: 1. a PDF file containing ESI† Sections S1–S6 (see DOI: **https://doi.org/10.1039/d5ce00367a**), and 2. raw spectroscopic, powder X-ray diffraction data and photocrystallographic data (in CIF format) are freely available *via* the Cardiff University Research Data Repository at **https://doi.org/10.17035/cardiff.29421074**.

Author contributions

The manuscript was written through contributions from all of the authors. All authors have given approval to the final version of the manuscript. Lauren Hatcher: conceptualization, methodology, visualization, writing – review & editing, supervision, project administration and funding acquisition. Sam Lewis: formal analysis, investigation, methodology, validation, data curation, writing – original draft preparation. Ben Coulson: formal analysis, visualization. Anna Warren: formal analysis, writing – review & editing. Kenneth Harris: supervision, writing – review & editing. Mark Warren: supervision, writing – review & editing.

Conflicts of interest

There are no conflicts to declare.

Acknowledgements

LEH and BAC are grateful to the Royal Society for support through LEH's University Research Fellowship (URF \R1\191104). SGL is supported by a joint studentship from Cardiff University, Diamond Light Source and the UK Hub for the Physical Sciences on XFELS (HPSX).

References

1 J. J. Morris, C. R. Bowen, B. A. Coulson, M. Eaton, P. R. Raithby, L. K. Saunders, J. M. Skelton, Q. Wang, M. R. Warren, Y. Zhang and L. E. Hatcher, *Angew. Chem., Int. Ed.*, 2024, **63**, e202401552.
2 R. Kulmaczewski, E. Trzop, E. Collet, S. Vela and M. A. Halcrow, *J. Mater. Chem. C*, 2020, **8**, 8420–8429.
3 M. Goulkov, D. Schaniel and T. Woike, *J. Opt. Soc. Am. B.*, 2010, **27**, 927–932.
4 D. Schaniel, M. Imlau, T. Weisemoeller, T. Woike, K. W. Kramer and H. U. Güdel, *Adv. Mater.*, 2007, **19**, 723–726.
5 S.-M. Bak, Z. Shadike, R. Lin, X. Yu and X.-Q. Yang, *NPG Asia Mater.*, 2018, **10**, 563–580.
6 R. M. Main, S. M. Vornholt, C. M. Rice, C. Elliott, S. E. Russell, P. J. Kerr, M. R. Warren and R. E. Morris, *Commun. Chem.*, 2023, **6**, 44.
7 M. A. Garcia-Garibay, *Proc. Natl. Acad. Sci. U. S. A.*, 2005, **102**, 10771–10776.
8 G. R. Desiraju, *Chem. Commun.*, 1997, 1475–1482, DOI: **10.1039/A607149J**.
9 H. Sugiyama, I. Yoshida, K. Johmoto, Y. Ishimoto, A. Sekine and H. Uekusa, *Bull. Chem. Soc. Jpn.*, 2023, **97**(1), uoad018.
10 L. K. Saunders, H. Nowell, H. C. E. Spencer, L. E. Hatcher, H. J. Shepherd, L. H. Thomas, C. L. Jones, S. J. Teat, P. R. Raithby and C. C. Wilson, *CrystEngComm*, 2018, **20**, 3074–3083.
11 L. E. Hatcher and P. R. Raithby, *CrystEngComm*, 2017, **19**, 6297–6304.
12 C. L. Jones, J. M. Skelton, S. C. Parker, P. R. Raithby, A. Walsh, C. C. Wilson and L. H. Thomas, *CrystEngComm*, 2019, **21**, 1626–1634.
13 D. Yan, A. Delori, G. O. Lloyd, B. Patel, T. Friščić, G. M. Day, D.-K. Bučar, W. Jones, J. Lu, M. Wei, D. G. Evans and X. Duan, *CrystEngComm*, 2012, **14**, 5121–5123.
14 M. M. Billah, S. Das, A. R. Aad and R. Paul, *J. Mater. Res. Technol.*, 2022, **20**, 2094–2108.
15 A. A. Benzerga and N. F. Shaver, *Scr. Mater.*, 2006, **54**, 1937–1941.
16 C. L. Hobday, S. Krause, S. M. J. Rogge, J. D. Evans and H. Bunzen, *Front. Chem.*, 2021, **9**, 772059.
17 A. A. Tiba, A. V. Tivanski and L. R. MacGillivray, *Nano Lett.*, 2019, **19**, 6140–6143.
18 Q. Li, C. W. Kartikowati, S. Horie, T. Ogi, T. Iwaki and K. Okuyama, *Sci. Rep.*, 2017, **7**, 9894.
19 Z. Chen, F. Li, Q. Huang, F. Liu, F. Wang, S. P. Ringer, H. Luo, S. Zhang, L.-Q. Chen and X. Liao, *Sci. Adv.*, 2020, **6**, eabc7156.
20 P. Coppens, *Angew. Chem., Int. Ed.*, 2009, **48**, 4280–4281.
21 P. R. Raithby, *Crystallogr. Rev.*, 2007, **13**, 121–142.
22 L. E. Hatcher, M. R. Warren, J. M. Skelton, A. R. Pallipurath, L. K. Saunders, D. R. Allan, P. Hathaway, G. Crevatin, D. Omar, B. H. Williams, B. A. Coulson, C. C. Wilson and P. R. Raithby, *Commun. Chem.*, 2022, **5**, 102.
23 T. Watanabe and H. Tanaka, *Synchrotron Radiat. News*, 2023, **36**, 3–6.
24 P. Raimondi, C. Benabderrahmane, P. Berkvens, J. C. Biasci, P. Borowiec, J.-F. Bouteille, T. Brochard, N. B. Brookes, N. Carmignani, L. R. Carver, J.-M. Chaize, J. Chavanne, S. Checchia, Y. Chushkin, F. Cianciosi, M. Di Michiel, R. Dimper, A. D'Elia, D. Einfeld, F. Ewald, L. Farvacque, L. Goirand, L. Hardy, J. Jacob, L. Jolly, M. Krisch, G. Le Bec, I. Leconte, S. M. Liuzzo, C.

Maccarrone, T. Marchial, D. Martin, M. Mezouar, C. Nevo, T. Perron, E. Plouviez, H. Reichert, P. Renaud, J.-L. Revol, B. Roche, K.-B. Scheidt, V. Serriere, F. Sette, J. Susini, L. Torino, R. Versteegen, S. White and F. Zontone, *Commun. Chem.*, 2023, **6**, 82.

25 APS Upgrade Project Final Design Review Report - 2019, **https://www.aps.anl.gov/APS-Upgrade/Documents**, accessed on 2nd April 2025.

26 Diamond II Advancing Science, Science Case 2019, **https://www.diamond.ac.uk/Home/About/Vision/Diamond-II.html**, Accessed on 2nd April 2025.

27 L. E. Hatcher, J. M. Skelton, M. R. Warren, C. Stubbs, E. L. da Silva and P. R. Raithby, *Phys. Chem. Chem. Phys.*, 2018, **20**, 5874–5886.

28 B. G. Abdallah, N. A. Zatsepin, S. Roy-Chowdhury, J. Coe, C. E. Conrad, K. Dörner, R. G. Sierra, H. P. Stevenson, F. Camacho-Alanis, T. D. Grant, G. Nelson, D. James, G. Calero, R. M. Wachter, J. C. H. Spence, U. Weierstall, P. Fromme and A. Ros, *Struct. Dyn.*, 2015, **2**, 041719.

29 C. Kupitz, I. Grotjohann, C. E. Conrad, S. Roy-Chowdhury, R. Fromme and P. Fromme, *Philos. Trans. R. Soc. B: Biol. Sci.*, 2014, **369**, 20130316.

30 L. E. Hatcher, W. Li, P. Payne, B. Benyahia, C. D. Rielly and C. C. Wilson, *Cryst. Growth Des.*, 2020, **20**, 5854–5862.

31 Z. Wu, S. Yang and W. Wu, *CrystEngComm*, 2016, **18**, 2222–2238.

32 L. H. Thomas, C. Wales, L. Zhao and C. C. Wilson, *Cryst. Growth Des.*, 2011, **11**, 1450–1452.

33 M. D. Carducci, M. R. Pressprich and P. Coppens, *J. Am. Chem. Soc.*, 1997, **119**, 2669–2678.

34 F. Bottomley and P. S. White, *Acta Crystallogr., Sect. B*, 1979, **35**, 2193–2195.

35 S. Horrell, D. Axford, N. E. Devenish, A. Ebrahim, M. A. Hough, D. A. Sherrell, S. L. S. Storm, I. Tews, J. A. R. Worrall and R. L. Owen, *J. Visualized Exp.*, 2021, **168**, e62200.

36 S. G. Lewis, B. A. Coulson, A. J. Warren, M. R. Warren and L. E. Hatcher, *Commun. Chem.*, 2024, **7**, 264.

37 P. Manoharan and W. C. Hamilton, *Inorg. Chem.*, 1963, **2**, 1043–1047.

38 I. Levin, *NIST Inorganic Crystal Structure Database (ICSD)*, National Institute of Standards and Technology, 2018, DOI: **10.18434/M32147**, (Accessed 2nd April 2025).

39 V. Angelidakis, S. Nadimi and S. Utili, *Powder Technol.*, 2022, **396**, 689–695.

40 C. F. Macrae, I. Sovago, S. J. Cottrell, P. T. A. Galek, P. McCabe, E. Pidcock, M. Platings, G. P. Shields, J. S. Stevens, M. Towler and P. A. Wood, *J. Appl. Crystallogr.*, 2020, **53**, 226–235.

41 R. Lacmann, A. Herden and C. Mayer, *Chem. Eng. Technol.*, 1999, **22**, 279–289.

42 A. S. Barnett, H. Nowell, R. M. Warren, A. Wilcox and R. D. Allan, *Protein Pept. Lett.*, 2016, **23**, 211–216.

43 D. Schaniel, J. Schefer, B. Delley, M. Imlau and T. Woike, *Phys. Rev. B*, 2002, **66**, 085103.

44 D. R. Lide, *CRC handbook of chemistry and physics: a ready-reference book of chemical and physical data, 2001–2002*, CRC Press, Boca Raton, 82nd edn, 2001.